

Magnetic properties of equiatomic CrMnFeCoNi

Timothy A. Elmslie,¹ Jacob Startt,² Sujeily Soto-Medina,³ Yang Yang,³ Keke Feng,⁴
Ryan E. Baumbach,⁴ Emma Zappala,⁵ Gerald D. Morris,⁶ Benjamin A. Frandsen,⁷
Mark W. Meisel,⁸ Michele V. Manuel,³ Rémi Dingreville,² and James J. Hamlin¹

¹Department of Physics, University of Florida, Gainesville, FL 32611, USA

²Center for Integrated Nanotechnologies, Sandia National Laboratories, Albuquerque, NM, 87185, USA

³Department of Materials Science and Engineering,
University of Florida, Gainesville, FL 32611, USA

⁴Department of Physics, Florida State University and National
High Magnetic Field Laboratory, Tallahassee Florida 32310, USA

⁵Department of Physics and Astronomy, Brigham Young University, Provo, Utah 84602, USA

⁶Centre for Molecular and Materials Science, TRIUMF, Vancouver, British Columbia V6T 2A3, Canada

⁷Department of Physics and Astronomy, Brigham Young University, Provo, Utah 84602, USA.

⁸Department of Physics and the National High Magnetic Field Laboratory,
University of Florida, Gainesville, Florida 32611, USA

(Dated: February 23, 2022)

Magnetic, specific heat, and structural properties of the equiatomic Cantor alloy system are reported for temperatures between 5 K and 300 K, and up to fields of 70 kOe. Magnetization measurements performed on as-cast, annealed, and cold-worked samples reveal a strong processing history dependence and that high-temperature annealing after cold-working does not restore the alloy to a “pristine” state. Measurements on known precipitates show that the two transitions, detected at 43 K and 85 K, are intrinsic to the Cantor alloy and not the result of an impurity phase. Experimental and *ab initio* density functional theory (DFT) computational results suggest that these transitions are a weak ferrimagnetic transition and a spin-glass-like transition, respectively, and magnetic and specific heat measurements provide evidence of significant Stoner enhancement and electron-electron interactions within the material.

I. INTRODUCTION

Investigation of high-entropy alloys began in the early 2000s with the work of Cantor, Kim, and Warren¹, who investigated multicomponent alloys of the formula $A_xB_{90-x}Al_{10}$, in which A and B each represented a combination of two to four different elements in equiatomic ratios. In this way, they were able to produce stable combinations of up to seven different elements. The phrase “high-entropy alloy,” however, was not introduced until 2004, in the work of Yeh *et al.*², who used it to describe compounds consisting of five or more elements. These alloys are of interest partly due to the extremely large number of new alloy systems which fall into the category of high or medium entropy alloys². Furthermore, prior investigations have revealed a number of alloys with intriguing properties such as high hardness and resistance to anneal softening², shape memory effects^{3,4}, and superconductivity⁵. Cantor alloys also have potential applications due to soft magnetism⁶ and other tunable magnetic properties⁷.

The specific combination of chromium (Cr), manganese (Mn), iron (Fe), cobalt (Co), and nickel (Ni) that would come to characterize the “Cantor alloy” was first identified in the 2004 work of Cantor, Chang, Knight, and Vincent⁸, who produced alloys of sixteen and twenty different elements in equal proportions through induction melting. The resulting compound was unsurprisingly multiphase, but the predominant phase was especially rich in Cr, Mn, Fe, Ni, and Co. In the same work, this

CrMnFeCoNi compound was identified as face-centered cubic (FCC), and the ability of this material to dissolve large amounts of elements such as niobium (Nb), titanium (Ti), and vanadium (V) was noted.

Much work has been done regarding the mechanical properties of Cantor alloys^{8–13}, as well as the magnetic properties of similar compounds^{6,7,14–23}, but fewer studies have examined the magnetic properties of the original CrMnFeCoNi alloy^{24–28}. Of its component elements, Cr and Mn are antiferromagnetic with $T_N = 311$ K²⁹ and $T_N = 100$ K³⁰ respectively, while Fe, Co, and Ni are ferromagnetic with $T_C = 1043$ K, $T_C = 1394$ K, and $T_C = 631$ K, respectively³¹. However, the magnetic transitions in the equiatomic Cantor alloy appear at much lower temperature. Jin *et al.*²⁴ identified a peak in the magnetization of CrMnFeCoNi at 25 K and suggested that it could be either an antiferromagnetic transition or a spin-glass transition. Schneeweiss *et al.*²⁶, however, found two transitions in the magnetization: a spin-glass transition at 93 K, and a ferromagnetic transition at 38 K. They were able to identify the 38 K transition as ferromagnetic by magnetic hysteresis loops after cooling in field, while the nature of the spin-glass transition was confirmed by magnetic moment relaxation measurements. Despite identifying these magnetic characteristics, the data of Schneeweiss *et al.* do not afford additional quantitative analysis since the magnetization results are only reported in units of emu, rather than in a generic manner like emu g^{-1} . Consequently, the identification of the atoms and/or atomic morphology gen-

erating the magnetic response is not quantitatively addressed, and this work provides insights about this important issue.

Kamarád *et al.*²⁷ investigated the magnetic properties of the equiatomic Cantor alloy between ambient pressure and 1 GPa, observing that increasing pressure decreased magnetization slightly. Using Curie-Weiss fitting, they found evidence of strong antiferromagnetic interactions, which were conjectured to be responsible for the observed small magnetization values as well as the linear field dependence of the magnetization. In contrast, while Schneeweiss *et al.* found ferromagnetic-type behavior in magnetic hysteresis loops after cooling in applied magnetic field, Kamarád *et al.* were unable to replicate these results, seeing a change of only 0.4 emu g^{-1} in magnetization after field-cooling. These observations led Kamarád *et al.* to disagree with Schneeweiss *et al.* on the nature of the magnetic transitions within the compound, identifying ferrimagnetic order below 85 K and magnetic cluster-glass behavior below 43.5 K.

This work reports a quantitative analysis of the magnetic properties of the equiatomic Cantor alloy CrMnFeCoNi based on a combination of compositional and structural characterization, magnetization studies, Hall effect measurements, muon spin relaxation (μSR) results, specific heat studies, and *ab initio* density functional theory (DFT) calculations. The magnetic response of as-cast, annealed, and cold-worked samples revealed a strong history dependence, which is described and contrasted with the magnetic properties of precipitates known to form in Cantor alloys. All of our results lead to the identification of the magnetic signatures as intrinsic characteristics of the equiatomic Cantor alloy CrMnFeCoNi, with weak ferrimagnetic order near 43 K, a spin-glass-like fingerprint near 85 K, and a sizable temperature-independent response. This latter contribution was established by Curie-Weiss analysis of the magnetic susceptibility data and further probed by Hall measurements to determine the expected size of the Pauli paramagnetic contribution to the susceptibility. Combined with an interpretation of the specific heat data and DFT results, our work provides evidence of a sizable Stoner enhancement and electron-electron interactions.

II. METHODS

A. Materials Synthesis and History

Samples were synthesized by combining stoichiometric amounts of elemental Cr, Mn, Fe, Co, and Ni and melting them together in an Edmund Bühler MAM-1 compact arc melter to produce as-cast samples. The Cr, Mn, Fe, and Ni elements were sourced from Alfa Aesar, while Co was purchased from Cerac. The Cr used for synthesis was 99.995% pure, while the Co was 99.5% pure. All other elements were 99.95% pure. Each sample was melted five times, flipping it over between each melt to improve

sample homogeneity. Samples measured immediately after arc-melting are referred to as “as-cast.” Annealed samples were made by sealing as-cast samples in quartz tubes under Ar atmosphere and homogenizing them at 1100 °C for 6 days, after which the tube containing the samples was quenched in water. Samples measured following this step are called “anneal A.” The piece cut from the as-cast boule and annealed in ambient atmosphere at 700 °C for one hour is referred to as “oxidized.” Some samples from the anneal A batch were cold-worked by flattening them in a hydraulic press a total of three times using a pressure of approximately 0.5 GPa, folding them in half between each flattening step. These samples are known as “cold-worked.” After cold-working, the samples were re-annealed in quartz tubes under argon (Ar) atmosphere. A portion were annealed at 700 °C for one hour, while others were again subjected to 1100 °C for six days, referred to as “anneal B” and “anneal C,” respectively.

B. Compositional and Structural Analysis

The microstructure of the sample was characterized using a Tescan MIRA3 scanning electron microscope (SEM) with an energy-dispersive X-ray (EDX) detector at 20 kV. Prior to SEM measurements, samples were mounted in resin epoxy and first polished using 600 grit, then 800 grit SiC paper. This surface was further polished using alcohol-based lubricant and diamond paste of varying particulate sizes in steps of 6 μm , 3 μm , 1 μm followed by 0.05 μm master polishing using water-free colloidal silica suspension. The crystal structure of the sample was investigated using a Panalytical Xpert Powder X-ray diffractometer (XRD) with a copper-radiation source at an accelerating voltage of 40 kV and an electron current of 40 mA, over a 2θ range from 40° to 120°. Powder samples were prepared using a mortar and pestle. Quantitative composition data were obtained by electron probe microanalysis (EPMA) using a CAMECA SX-FiveFE instrument operating with an accelerating voltage of 15 kV and a probe current of 20 nA.

C. Magnetic and Magnetotransport Studies

A Quantum Design Magnetic Property Measurement System (MPMS) was used to take magnetization data. Small pieces ranging from a few milligrams to a few hundred milligrams were cut from larger samples using an Allied 3000 low speed saw to minimize unintentional working of the samples. Each sample was secured in a gel capsule inside a plastic straw for measurement. In order to obtain magnetization versus temperature data, samples were cooled under zero field to a temperature of 5 K, after which field was applied and data was recorded while warming. This process produced the datasets labeled zero-field cooled (ZFC). The applied field was held

constant while the temperature warms to 300 K and subsequently cools to 5 K again. Then data was recorded while warming to produce field-cooled warming (FCW) datasets.

Resistivity and Hall measurements were performed in a Quantum Design Physical Property Measurement System (PPMS) at 300 K. For these measurements, an Allied 3000 low speed saw was used to cut an 8 mm by 8.4 mm flat square sample from the arc-melted boule. Then four notches, one on each side, were cut into it with the same device to produce a rough clover leaf shape for the purposes of Van der Pauw measurements. To increase the signal-to-noise ratio, the sample was first sanded on a custom jig to a thickness of 0.2 mm, then polished with 800 grit silicon carbide paper to a final thickness of 0.16 mm. This sample was placed on a PPMS transport puck with a piece of cigarette paper between sample and puck for insulation, while N-grease provided thermal contact. Each “leaf” of the clover-like shape of the sample was connected to one of the puck solder pads using platinum wire affixed to the sample with silver paint.

D. Muon spin relaxation experiments

Muon spin spectroscopy measurements, or μ SR, were conducted to probe the spin dynamics and provide sensitivity to the volume fraction of the various magnetic phases in equiatomic Cantor alloy. These experiments were conducted at TRIUMF Laboratory in Vancouver, Canada using the LAMPF spectrometer on the M20D beamline. Positive muons with 100% initial spin polarization were implanted one at a time in the sample. After implantation, the muon spin underwent Larmor precession in the local magnetic field at the muon site, which consists of the vector sum of the internal magnetic field due to electronic and/or nuclear dipolar moments and any externally applied magnetic field. After a mean lifetime of 2.2 μ s, the muon decays into two neutrinos and a positron, with the latter being emitted preferentially in the direction of the muon spin at the moment of decay. Two detectors placed on opposite sides of the sample record positron events as a function of time after muon implantation, yielding the μ SR asymmetry $a(t) = [N_1(t) - N_2(t)]/[N_1(t) + N_2(t)]$, where $N_1(t)$ and $N_2(t)$ are the number of positron events recorded at time t . This quantity is proportional to the projection of the muon ensemble spin polarization along the axis defined by the positions of the detectors, from which information about the local magnetic field distribution in the sample can be inferred³². The sample was mounted on a low background copper sample holder, and the temperature controlled using a helium gas flow cryostat. The μ SR data were analyzed using the open source programs MusrFit³³ and BEAMS³⁴, which yield consistent results. The correction parameter α was determined according to standard practice from a weak transverse field measurement in the paramagnetic state³⁵.

E. Specific Heat Measurements

Alloy specific heat was measured in a PPMS with the attached PPMS heat capacity option in order to obtain the Debye temperature and the approximate magnetic entropy of the sample. The sample used for specific heat measurements was annealed at 1100 °C for six days before being cut to a mass of a few milligrams using an Allied 3000 low speed saw to minimize sample deformation and strain. After cutting, this piece was placed on the sample platform of a Quantum Design heat capacity puck using a small amount of Apeizon N grease to adhere the sample and provide thermal contact before being inserted into the PPMS for measurement.

F. DFT Calculations

Spin collinear DFT simulations were performed to investigate exchange splitting between spin states and its effect on ferromagnetism within the system. For modeling, the Vienna ab-initio Simulation Package (VASP)^{36–38} was used, in which the electronic wavefunctions were modeled through plane-waves and projector-augmented wave (PAW) pseudopotentials^{39,40}. Exchange-correlation effects were treated within the generalized gradient approximation (GGA) according to the parametrization of Perdew, Burke, and Ernzerhof (PBE)⁴¹, while the individual pseudopotentials used to model each species were chosen so that only the outermost s - and d -valence electrons were explicitly included.

The alloy atomic structure was modeled using supercells containing 108 atoms – representing a $3 \times 3 \times 3$ transformation of the conventional four atom FCC unit cell. Special quasi-random structures (SQS)^{42,43}, built using the openly available Alloy-Theoretic Automated Toolkit (ATAT)⁴⁴, were used to replicate random atomic ordering among lattice sites. To ensure the most accurate description of properties of the randomly ordered solid solution structure, four separate 108 atom SQS supercells were modeled at the equiatomic composition, each using a $5 \times 5 \times 5$ gamma-centered k-point mesh. For all simulations, electronic convergence was met when the total energy of the system fell below 1.0×10^{-6} eV, while ionic convergence was met when forces on all atoms fall below 20×10^{-3} eV \AA^{-1} . Lastly, a plane-wave energy cutoff of 400 eV was found to sufficiently minimize the total energy when used with a Gaussian smearing method and a smearing width of 0.01 eV.

III. EXPERIMENTAL RESULTS

A. Microstructural Analysis

A representative example of the microstructure of the Cantor alloy samples is shown in Fig. 1 for the anneal

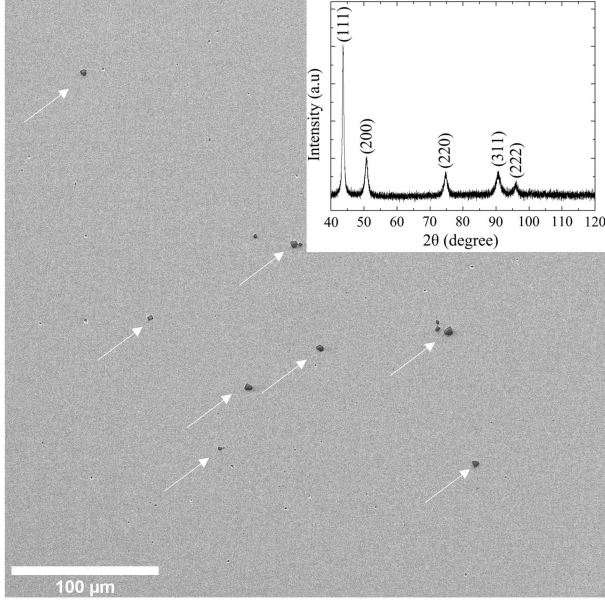


FIG. 1: SEM image of homogenized Cantor alloy (anneal A). A small number of particles (black spots identified by arrows) were determined by EDX to be oxide rich in Cr and Mn. The XRD data indicated the sample is single-phase and all peaks could be indexed as FCC.

A sample. The micro-sized pores observed in the SEM image are considered to be casting porosity. Additionally, EDX analysis identified a small number of particles as oxides rich in Cr and Mn. The sample consists of a single FCC phase according to the XRD pattern, and no peak was identified as corresponding to the oxide particles. The existence of such (Cr, Mn)-rich particles in as-cast and homogenized Cantor alloys have been reported in previous studies^{45–47}. Furthermore, the XRD data did not contain any peaks associated with inclusions⁴⁸, which, due to their small volume fraction, are not considered to significantly influence the properties reported later in this work. Sample composition was confirmed via an EPMA measurement of the as-cast sample, and the results are presented in Table I.

TABLE I: Composition of the as-cast equiatomic Cantor alloy, as determined by EPMA measurement.

Element	at. %
Cr	20.31 ± 1.05
Mn	19.44 ± 2.01
Fe	20.48 ± 1.32
Co	20.13 ± 0.83
Ni	19.65 ± 0.99

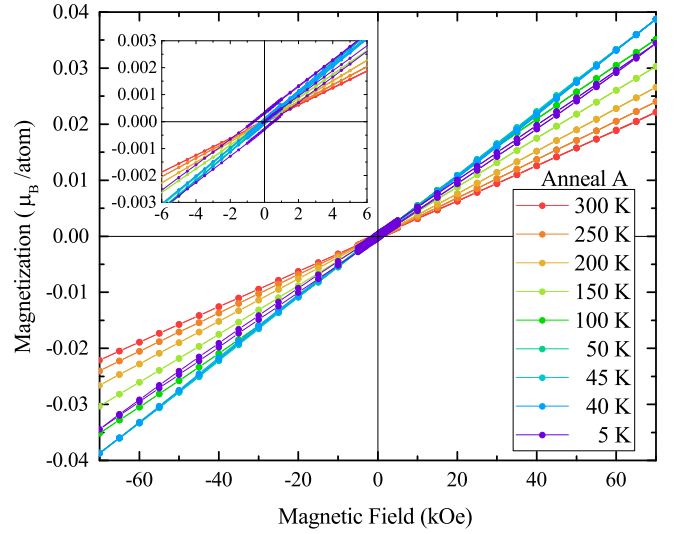


FIG. 2: Magnetization versus field data on equiatomic Cantor alloy at a variety of temperatures between 5 K and 300 K. Inset shows the same data at low field, between -6 kOe and 6 kOe. The magnetization remains small to the highest measured fields.

B. Magnetization of Homogenized CrMnFeCoNi

A magnetization versus temperature plot for a sample of equiatomic Cantor alloy at different temperatures from 5 K to 300 K is displayed in Fig. 2. All of the displayed curves remain roughly linear across the measured range of -70 kOe to 70 kOe with magnitudes of only a few hundredths of a bohr magneton, demonstrating that the compound is far from magnetic saturation. The only feature that clearly distinguishes one curve from another is the temperature dependence as indicated by different slopes for different temperatures. The 300 K dataset has the lowest slope, and slope increases as temperature decreases until 40 K and 45 K, which largely overlap one another. As temperature falls below 40 K, the slope begins to decrease again.

Field-cooled warming (FCW) magnetization versus temperature data from a sample of anneal A are displayed in Fig. 3 at fields from 0.1 kOe to 20 kOe, while the inset compares both zero-field cooled (ZFC) and FCW data at 0.1 kOe. Magnetization plots are presented in units of $\text{emu mol}_{\text{atom}}^{-1} \text{Oe}^{-1}$ to simplify estimation of effective moment, p_{eff} , which can be written as

$$p_{\text{eff}} = 2.82 C_m^{1/2}, \quad (1)$$

where p_{eff} is in units of bohr magnetons and C_m is the Curie constant in units of $\text{emu K mol}_{\text{atom}}^{-1} \text{Oe}^{-1}$ ⁴⁹. In this notation, mol_{atom} denotes moles of atoms, as opposed to, for example, moles of formula units or moles of magnetic ions, and emu is defined as erg G^{-1} , as reported by the Quantum Design MPMS. At 0.1 kOe, two transitions are clearly seen: a step-like anomaly at 43 K, and a peak at 85 K. As field increases, the 43 K transition

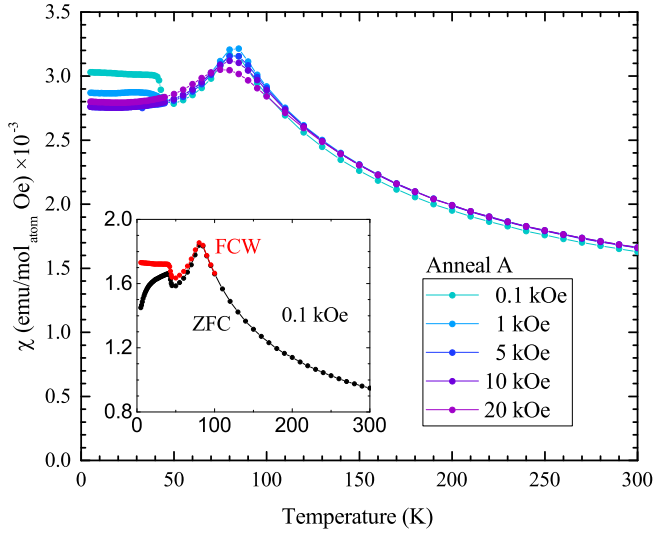


FIG. 3: Magnetic susceptibility versus temperature data on equiatomic Cantor alloy under various applied magnetic fields. The main plot shows only field-cooled warming (FCW) data, while the inset shows compares zero-field cooled (ZFC) and FCW data at 0.1 kOe.

is rapidly suppressed, becoming notably smaller at 1 kOe and vanishing completely at 5 kOe and above. The higher temperature transition is less affected by the increase in field. At an applied field of 20 kOe, the higher temperature transition is slightly smaller, slightly broadened and shifted down in temperature from 85 K to 75 K compared to the 0.1 kOe curve. The small size of the 43 K transition is notable, which led us to examine the possibility that it could derive from one of the known impurity phases^{46,50,51}.

C. Effects of Plastic Deformation

Since the Cantor alloy is known to form precipitates as a result of deformations and moderate temperature anneals^{46,50,51}, investigation of the processing history dependence of the compound is necessary in order to understand the origin of the magnetic behavior. The 43 K transition in particular is notably small, with step size of approximately $1 \times 10^{-5} \mu_B \text{ atom}^{-1}$ in fields of 0.1 kOe and 1 kOe, suggesting that it may originate from a magnetic secondary phase which comprises a proportionally small amount of the sample. This hypothesis is tested through magnetization measurements performed on samples which have undergone different cold-working and annealing processes. The data are plotted in Fig. 4, in which each curve represents a different processing history, as described in the Methods section. In Fig. 4A, the as-cast sample shows a large 43 K transition relative to the other samples, but notably lacks a peak at higher temperature. Annealing the as-cast material at 1100 °C produces the anneal A sample, in which the 45 K signature is significantly smaller and sharper than the corresponding

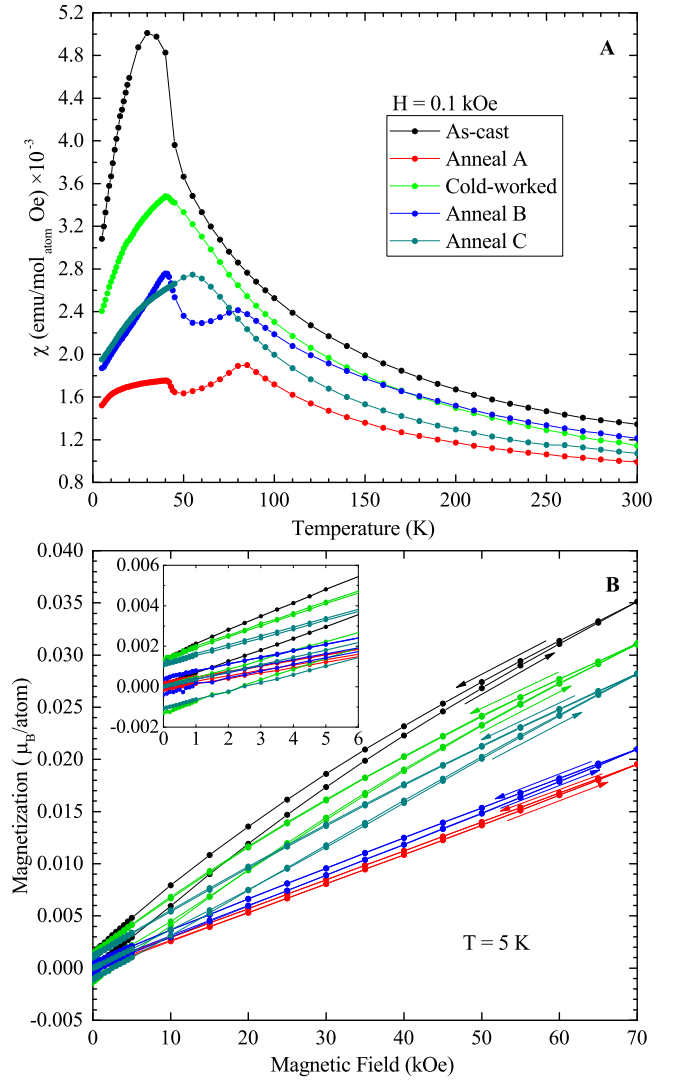


FIG. 4: Effects of annealing and cold working on the magnetic properties of equiatomic Cantor alloy. (A) ZFC susceptibility as a function of temperature at 0.1 kOe. (B) Magnetization as a function of magnetic field at 5 K. Data are plotted in units of bohr magnetons per atom to show that the compounds are not close to saturation across the range of measured magnetic field. Larger hysteresis in the cold-worked and anneal C samples may be indicative of ferromagnetic precipitates. Inset shows the same datasets at low field, up to 6 kOe.

feature in the as-cast sample. Additionally, a sharp peak appears at 85 K in the anneal A data. Further changes of the magnetic response are observed after cold-working the anneal A sample in a hydraulic press (cold-worked), and subsequently, annealing at 700 °C for one hour (anneal B), and at 1100 °C for six days (anneal C). These datasets demonstrate that cold-working reduces the size of the 43 K transition and pushes the higher temperature transition to lower temperatures while increasing its size. However, annealing, even for a brief duration, results in a 43 K transition larger than what appears in the cold-worked samples but smaller than that of the arc-

melted as-cast. In addition, in moving from the as-cast to the annealed samples, the higher temperature transition is revealed, even if it remains smaller than in the cold-worked sample. This strong processing dependence also explains differences between the results of our measurements and those of others^{24,26,27}.

Magnetization versus magnetic field data for the same samples are shown in Fig. 4B, using the same color-coding as Fig. 4A. The data are plotted in units of bohr magnetons per atom to clearly demonstrate that none of the measured samples are close to magnetic saturation up to fields of 70 kOe. Furthermore, these datasets show the magnetization of processed samples are similar in magnitude to those of the ‘pristine’ annealed sample. The inset plot shows a detailed view of low-field data below 6 kOe. Anneal A reveals the lowest level of hysteresis, while the cold-worked and anneal C samples show the highest. Larger hysteresis may be indicative of the emergence of ferromagnetic secondary phases.

D. Impurity Contribution to Magnetic Properties

Having investigated the effects of different processing steps on the equiatomic Cantor alloy itself, the next step was to synthesize and measure the magnetism of the precipitates, shown in Fig. 5, with the annealed equiatomic, NiMn, and NiMn+(Cr,Fe,Co)_ε on the left y-axis of Fig. 5A and FeCo and FeCo+(Cr,Mn,Ni)_ε on the right axis. Despite synthesizing and annealing in Ar atmosphere, oxidation of the alloy is also considered, and data from the oxidized sample are also included on the left axis of pannel A. Measurements performed on the Cr-rich precipitate reveal magnetization values significantly higher than those of the NiMn compounds and significantly lower than the FeCo compounds, such that the Cr compound data do not fit easily alongside either. For clarity, this curve has been separated into pannel B, where it is compared to anneal A independently. The suffixes of “+(Cr,Fe,Co)_ε,” “+(Cr,Mn,Ni)_ε” and “+(Mn,Fe,Co,Ni)_ε” indicate the presence of small amounts of other Cantor alloy elements added to match the compositions of precipitates reported by Otto *et al.*⁴⁶, Schuh *et al.*⁵⁰, and Li *et al.*⁵¹. The investigated precipitates lack any signs of a transition near 43 K, suggesting that this transition is, in fact, an intrinsic aspect of the Cantor alloy system. While the 85 K transition is present in the oxidized curve, its size is not significantly changed relative to the anneal A curve. Furthermore, this transition is also not present in any of the precipitate curves, suggesting that it is also intrinsic to the Cantor alloy.

E. Muon Spin Relaxation

Key experimental results from the μ SR measurements of a sample from anneal A are shown in Fig. 6. Panel A displays asymmetry spectra collected at representative

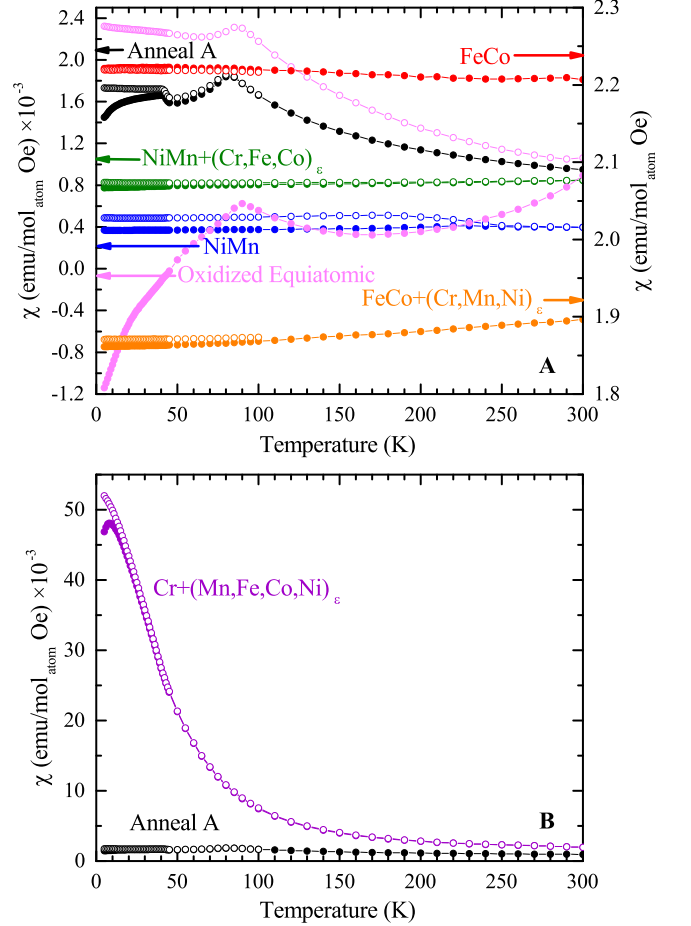


FIG. 5: (A) Comparison of magnetic susceptibility versus temperature data from FeCo and NiMn precipitate compounds as well as an oxidized equiatomic compound and anneal A. FeCo-based compounds exhibit comparatively large magnetization and are measured on the right y-axis for clarity. (B) Comparison of magnetic susceptibility data from the Cr-rich precipitate compound and anneal A. The “+(Cr,Fe,Co)_ε,” “+(Cr,Mn,Ni)_ε” and “+(Mn,Fe,Co,Ni)_ε” suffixes indicate the presence of small amounts of other Cantor alloy elements consistent with the precipitate compositions observed in the works of Otto *et al.*⁴⁶, Schuh *et al.*⁵⁰, and Li *et al.*⁵¹. Closed circles represent zero-field cooled (ZFC) data, while open circles represent field-cooled warming (FCW) data. All data is measured in emu per moles of atoms per Oe.

temperatures between 2 K and 153 K. At the highest temperature studied, a gentle relaxation with a Gaussian-like nature is observed. Applying a field of 1 kOe parallel to the initial muon spin polarization recovers approximately 75% of the asymmetry (data not shown), indicating that the relaxation at this temperature is due primarily to weak, random dipolar fields from nuclear moments⁵². As the temperature is lowered, the relaxation increases and becomes more exponential in nature, characteristic of magnetic fluctuations from electronic spins. Between 87 K and 82 K, the initial asymmetry drops

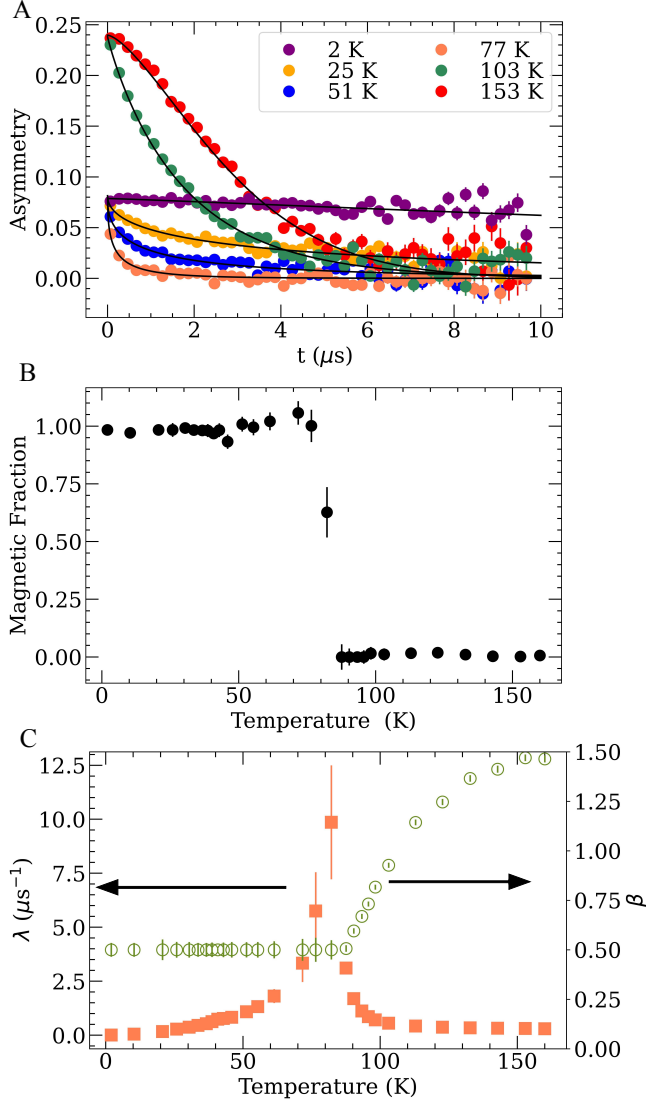


FIG. 6: (a) Representative μSR asymmetry spectra collected at various temperatures in zero field. The colored symbols show the data, and the black solid curves show the fits described in the main text. (b) Temperature dependence of the volume fraction of the sample exhibiting static magnetism. (c) Temperature dependence of the relaxation rate λ (left vertical axis) and relaxation exponent β (right vertical axis) determined from fits to the asymmetry spectra.

rapidly from ~ 0.24 to ~ 0.135 and then further to 0.08 (i.e., $1/3$ the total initial asymmetry) at 77 K. This “ $1/3$ tail” is the hallmark of a polycrystalline material with static magnetism throughout the full sample volume. No coherent oscillations of the asymmetry are observed in the “ $2/3$ component”, indicating very large fields and/or a broad distribution of field strengths at the muon stopping sites⁵². As the temperature is lowered further, the relaxation of the $1/3$ component gradually slows until almost no relaxation remains at 2 K, consistent with magnetic fluctuations freezing out. Qualitative inspection of

the spectra therefore confirms the presence of a sharp and uniform transition throughout the full sample volume with an onset temperature between 82 and 87 K. No pronounced change in the spectra is observed around 43 K, which demonstrates the transition at this temperature cannot be due simply to a minority phase in the sample, otherwise a further drop of the asymmetry would be observed below 43 K.

To gain more quantitative insight, least-squares fits to the asymmetry data were performed using the stretched exponential function $a(t) = a_0 e^{(-\lambda t)^\beta}$, where $a(t)$ is the time-dependent asymmetry, a_0 is the initial asymmetry at $t = 0$, λ is the relaxation rate, and β is the exponential power. This type of stretched exponential function is phenomenological, employed to model a continuous distribution of relaxation rates⁵³. The best-fit asymmetry curves agree well with the data, as seen by the solid curves in Fig. 6A. The volume fraction of the sample that exhibits static magnetism can be determined from the initial asymmetry values as $f(T) = (a_0^{\text{max}} - a_0(T)) / (a_0^{\text{max}} - a_0^{\text{LT}})$, where $a_0(T)$ is the best-fit value of a_0 at temperature T , and a_0^{max} is the maximum value of a_0 across all measured temperatures, and a_0^{LT} is the average value of a_0 for the low-temperature data ($T < 70$ K). As seen in Fig. 6B, $f(T)$ transitions rapidly from 0 to 1 in a small temperature window centered around 82 K, indicating that the sample undergoes a highly uniform magnetic transition. Evidence of this transition is also shown in Fig. 6C, which displays the relaxation rate λ and the exponential power β as a function of temperature. The prominent peak in λ centered around 82 K is evidence of critical spin dynamics as the temperature decreases toward the transition, as is observed in canonical spin glasses and continuous phase transitions^{35,54}. The exponential power β is ~ 1.5 at high temperature where relaxation from nuclear dipolar fields dominates, but it decreases steadily as the temperature is lowered and electronic spin fluctuations become more prominent. At the transition temperature and below, β converges to values between 0.45 and 0.55 when left fully unconstrained, and for consistency, β was set to 0.5 for the spectra collected at 82 K and below. This value of β is expected when the system exhibits multiple relaxation channels and/or spin fluctuation rates⁵⁵, which is unsurprising in this highly disordered alloy. Similar values were also observed in the entropy-stabilized antiferromagnetic oxide $(\text{Mg},\text{Co},\text{Ni},\text{Cu},\text{Zn})\text{O}$ ⁵⁶.

F. Specific Heat

Specific heat data are used in later sections to calculate magnetic entropy and the effective mass of charge carriers in order to better understand the nature of the magnetism present in the Cantor alloy. Results of specific heat versus temperature measurements on the anneal A sample are shown in Fig. 7. Data collection focused on the regions around 43 K and 85 K, but no features are

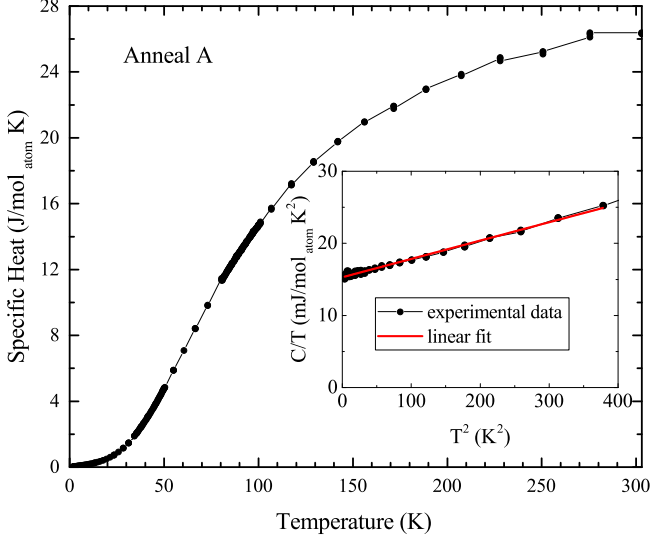


FIG. 7: Specific heat as a function of temperature for equiatomic Cantor alloy sample anneal A. Inset shows a plot of specific heat divided by temperature versus temperature squared.

apparent in this plot despite the transitions visible in the magnetization data at these temperatures. The inset contains a plot of C/T versus T^2 , focusing on the low-temperature region. The linear fit included in the inset follows from

$$C = \gamma T + \beta_{\text{ph}} T^3, \quad (2)$$

the expression for the low-temperature specific heat of a metal⁵⁷. In this equation, the γT term represents the electronic component of the specific heat, while $\beta_{\text{ph}} T^3$ is the lattice specific heat and is related to the Debye temperature. The results of fitting this equation are

$$\begin{aligned} \gamma &= 15.3(2) \text{ mJ mol}_{\text{atom}}^{-1} \text{ K}^{-2} \\ \beta_{\text{ph}} &= 0.025(3) \text{ mJ mol}_{\text{atom}}^{-1} \text{ K}^{-4}. \end{aligned}$$

G. Hall Effect and Carrier Density

Measurements of Hall voltage as a function of magnetic field permit the estimation of carrier density according to

$$V_H = \frac{IB}{ned}, \quad (3)$$

where I is the current, B is the magnetic field perpendicular to the current, e is the electron charge, and d is the sample thickness. The carrier density can, in turn, provide insight into the magnetism of the alloy as carried out in Section IV C. Results of Hall measurements are shown in Fig. 8, including a linear fit with a slope of $1.4(4) \times 10^{-4} \text{ nV Oe}^{-1}$. Using this slope in combination with Eq. 3, a carrier density $n = 2.9(8) \times 10^{22} \text{ cm}^{-3}$

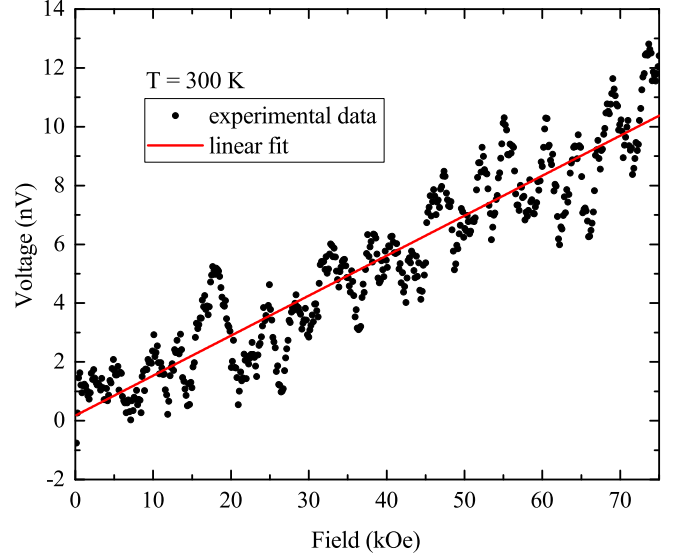


FIG. 8: Hall voltage of the equiatomic Cantor alloy sample anneal A. Data has been anti-symmetrized to remove any r_{xx} contribution.

can be calculated. This result is consistent with the carrier density of $\text{Al}_x\text{CrFeCoNi}$ reported by Kao *et al.*¹⁶, as well as with that of a typical metal ($\sim 1 \times 10^{22} \text{ cm}^{-3}$ to $1 \times 10^{23} \text{ cm}^{-3}$)^{58,59}.

IV. DISCUSSION

Experimental results reported in this work demonstrate the effects of processing on the two observed transitions in the equiatomic Cantor alloy as well as the intrinsic nature of these transitions. However, the magnetic properties can be examined in more detail, and information on the nature of magnetism in this sample can be extracted from the presented experimental data. This section begins with Curie-Weiss analysis of the magnetic susceptibility which reveals a significant constant offset. Analysis which combines specific heat data, computational results, and Hall measurements points to Stoner enhancement as the origin of the offset. The Stoner enhancement parameter Z is calculated through three different methods which obtain a Z value between 0.92 and 0.97, suggesting that this compound is on the cusp of magnetic order. This result is perhaps unsurprising given the observed magnetic transitions and the strong magnetic ordering seen in the Cantor alloy's constituent elements, but more notable is the small size of the magnetic transitions, which may be due to the presence of antiferromagnetic interactions, as evidenced by DFT results. These findings are consistent with previous work on a similar compound, $\text{Fe}_{40}\text{Mn}_{40}\text{Cr}_{10}\text{Co}_{10}$ ⁶⁰.

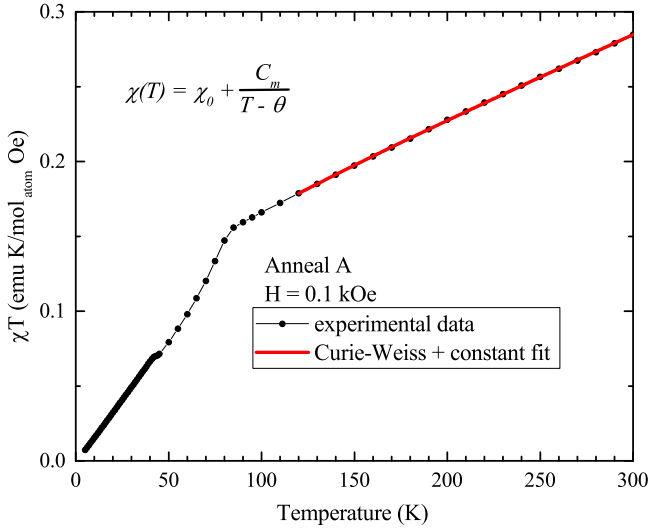


FIG. 9: Susceptibility times temperature versus temperature plot for equiatomic Cantor alloy, alongside a modified Curie-Weiss plus constant fit. The two transitions can be observed as sharp changes in slope. Above the 85 K transition, the plot is roughly linear with a positive slope.

A. Modified Curie-Weiss Fitting

When using a Curie-Weiss expression to estimate the effective moment of the anneal A sample at temperatures above the 85 K transition, reasonable fits required a modified expression written as

$$\chi(T) = \chi_0 + \frac{C_m}{T - \theta}, \quad (4)$$

where C_m is the Curie constant, θ is the Curie temperature, and χ_0 is a temperature-independent constant. This dataset is plotted as susceptibility times temperature for greater readability across the entire temperature range. The resulting fit is compared with experimental data in Fig. 9, and the resultant value for each parameter is listed in Table II.

TABLE II: Constant offset χ_0 , Curie constant C_m , Curie temperature θ , and effective moment p_{eff} from modified Curie-Weiss fit, Eq. 4. The value of p_{eff} was calculated using Eq. 1 and the value of C_m .

Variable	Value	Units
χ_0	5.4×10^{-4}	$\text{emu mol}_{\text{atom}}^{-1} \text{Oe}^{-1}$
C_m	0.13	$\text{emu K mol}_{\text{atom}}^{-1} \text{Oe}^{-1}$
θ	-16.1	K
p_{eff}	1.01	$\mu_B \text{ atom}^{-1}$

This fitting equation and its results differ notably from those of Kamarád *et al.*,²⁷ who used a non-modified Curie-Weiss equation to obtain a Curie temperature of $\theta = -210$ K and an effective moment of $p_{\text{eff}} = 2.71 \mu_B/\text{f.u.}$, using their formula of

$\text{Cr}_{0.205}\text{Mn}_{0.20}\text{Fe}_{0.205}\text{Co}_{0.199}\text{Ni}_{0.191}$. Given the strong history dependence of the Cantor alloy, this discrepancy may be a result of the differing processing methods, since Kamarád *et al.* cold-rolled their samples after casting and then annealed at 1173 K for 1 h. Our investigation of Cantor alloy processing history dependence shows that cold-working will increase magnetization, and subsequent high-temperature annealing will not restore the sample to a “pristine” state.

B. Specific Heat and Entropy

The fit in Fig. 7 provides the parameter β , which is the coefficient of the phonon contribution to the specific heat. In the low-temperature limit, β can be used to calculate the Debye temperature Θ_D according to

$$\beta = \frac{12\pi^4}{5} \frac{N_A k_B}{\Theta_D^3}, \quad (5)$$

in which N_A is Avogadro’s number⁶¹. This calculation gives $\Theta_D = 427$ K, not far from the Debye temperatures of some of the Cantor alloy’s component elements⁶². The Debye temperature can also be estimated by visual comparison of the phononic component of the specific heat to the Debye function, plotted as C versus T/Θ_D ⁵⁷. If Θ_D is chosen correctly, the two curves should closely align. The phononic specific heat is estimated by subtracting γT from the experimentally obtained specific heat, with the value of γ taken from the fit shown in the inset of Fig. 7. This process produces a Debye temperature $\Theta_D = 380$ K. These values are displayed in Table III for comparison.

TABLE III: Debye temperatures of the equiatomic Cantor alloy and its component elements. Elemental Debye temperatures are obtained from Kittel⁶².

Compound	Θ_D (K)
CrMnFeCoNi, Eq. 5	427
CrMnFeCoNi, Debye function comparison	380
Cr	630
Mn	410
Fe	470
Co	445
Ni	450

An estimate of the magnetic entropy of the equiatomic Cantor alloy is shown in Fig. 10, while the inset contains the magnetic component of the specific heat divided by temperature as a function of temperature. In order to determine the magnetic contribution, the specific heat of Fe as a function of temperature was compiled from multiple sources^{63–65} in the assumption that it would approximate the phononic component of the specific heat in the Cantor alloy. The Fe data were smoothed, then rescaled by a factor of 403/470 to account for differences in Debye temperatures between the equiatomic Cantor alloy and elemental Fe. Since two different values of the Cantor

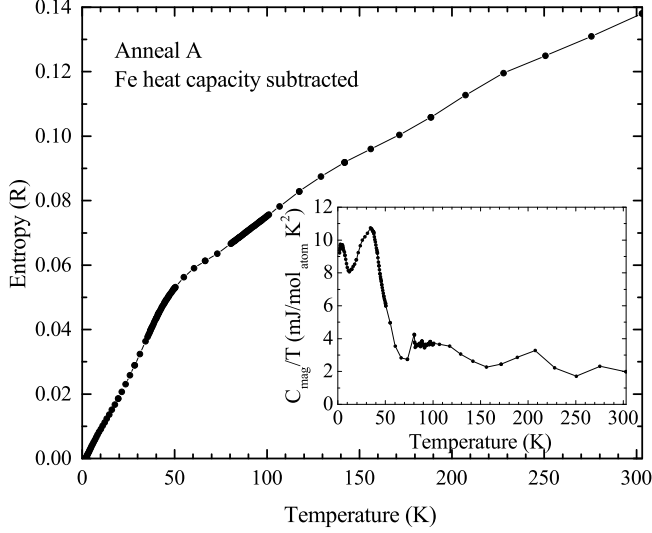


FIG. 10: Magnetic entropy as a function of temperature in units of R , the gas constant. The inset plot shows an estimate of the magnetic component of the specific heat produced by subtracting rescaled Fe specific heat data from the Cantor alloy specific heat data shown in Fig. 7.

alloy Debye temperature are obtained through different methods, this ratio uses the average of these values. The re-scaled fit data were subtracted from the specific heat data shown in Fig. 7, and the results are shown in Fig. 10 in the form of C_{mag}/T versus T . Integrating over the magnetic specific heat divided by temperature gives the entropy associated with magnetism in the Cantor alloy.

C. Effective Mass and Carrier Density

The fit shown in Fig. 7 to the specific heat also provides an estimation of the electronic contribution through the coefficient γ . This value can be used to calculate the effective carrier mass m^* according to

$$\frac{m^*}{m_e} = \frac{\gamma}{\gamma_0}, \quad (6)$$

in which m_e is the mass of a free electron⁵⁷. The variable γ_0 is a theoretical value calculated from the electronic DOS and can be expressed as

$$\gamma_0 = (\pi k_B)^2 \frac{g(E_F)}{3}, \quad (7)$$

in which k_B is the Boltzmann constant and $g(E_F)$ is the DOS in the d -band at the Fermi level, E_F ⁶⁶. In metals such as the Cantor alloy studied here, the s - and p -bands are broad near the Fermi level and thus contribute very little to the overall electron occupation. In other words, only the d -band needs to be taken into account⁶⁷. The spin separated projected DOS of the d -band, taken from the combined DOS of the four DFT calculations in

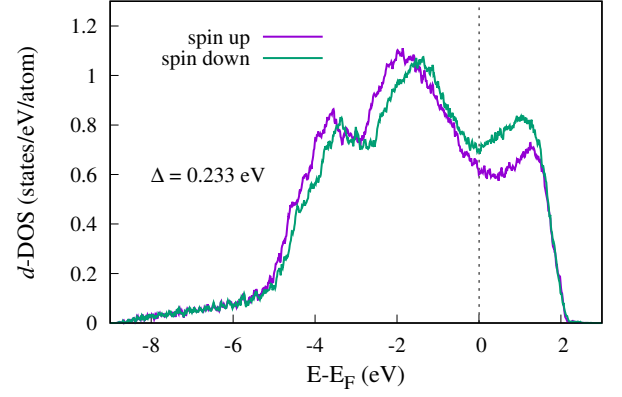


FIG. 11: The d -projected total density of states calculated from DFT. The spin-up states are shown by the purple line while spin-down states are shown using green. The Δ value is the exchange splitting parameter needed to evaluate the Stoner Criterion and represents the splitting in energy between the up and down states. This result is calculated by measuring the average separation (in eV) of the identifiable peaks and features in the occupied region of the DOS (*i.e.*, below the Fermi level). These DOS curves represent a combination of the individual DOS plots from each DFT simulation, normalized for the total number of atoms.

this work, and normalized to a per atom occupation is presented in Fig. 11. The spin-up and spin-down occupations at the Fermi energy are $0.613 \text{ states eV}^{-1}\text{atom}^{-1}$ and $0.736 \text{ states eV}^{-1}\text{atom}^{-1}$, respectively, resulting in a combined total Fermi level occupation of $g(E_F) = 1.349 \text{ states eV}^{-1}\text{atom}^{-1}$. Using this total Fermi level into Eq. 7, one finds $\gamma_0 = 3.18(9) \text{ mJ mol}_{\text{atom}}^{-1} \text{ K}^{-2}$, leading to an effective carrier mass of $m^* = 4.8(1) m_e$.

This analysis can be extended by first examining the results provided by the Hall studies which provide a carrier density $n = 2.9(8) \times 10^{22} \text{ cm}^{-3}$. Combined with a value of the effective mass m^* extracted from the specific heat, estimates of the Fermi energy

$$E_F = \frac{\hbar^2}{2m^*} (3\pi^2 n)^{2/3}, \quad (8)$$

and the Pauli paramagnetic susceptibility

$$\chi_P = \frac{3n\mu_0\mu_B^2}{2E_F}, \quad (9)$$

yield $E_F = 0.72(8) \text{ eV}$ and $2.3(2) \times 10^{-5} \text{ emu mol}_{\text{atom}}^{-1} \text{ Oe}^{-1}$, respectively. By comparison, fitting experimental susceptibility data yielded a constant offset of $5.4 \times 10^{-4} \text{ emu mol}_{\text{atom}}^{-1} \text{ Oe}^{-1}$, as seen in Table II. A diamagnetic contribution to the temperature independent part of the susceptibility is also expected, consisting of Landau diamagnetic and core diamagnetic components⁶⁸. Landau diamagnetic susceptibility can be determined by

$$\chi_L = -\frac{1}{3} \frac{m_e^2}{m^{*2}} \chi_P, \quad (10)$$

which produces a value of $\chi_L = -3.3(3) \times 10^{-7} \text{ emu mol}_{\text{atom}}^{-1} \text{ Oe}^{-1}$.⁶⁸ The core diamagnetism depends on the ionization of the atoms within the compound⁶⁹, which is currently not known. However, based on the possible ionization states of Cr, Mn, Fe, Co, and Ni, the core diamagnetic susceptibility χ_{core} must be between $-6.0 \times 10^{-7} \text{ emu mol}_{\text{atom}}^{-1} \text{ Oe}^{-1}$ and $-1.1 \times 10^{-6} \text{ emu mol}_{\text{atom}}^{-1} \text{ Oe}^{-1}$. These estimates suggest that the effects of Landau diamagnetism are negligible in the overall susceptibility of the equiatomic Cantor alloy, and the core diamagnetism may account for at most a 5% reduction in the temperature-independent susceptibility.

A value for the Pauli paramagnetic susceptibility can also be determined from first principles methods according to⁷⁰

$$\chi_P = \mu_0 \mu_B^2 g(E_F). \quad (11)$$

This equation gives a Pauli paramagnetic susceptibility of $4.4 \times 10^{-5} \text{ emu mol}_{\text{atom}}^{-1} \text{ Oe}^{-1}$, similar to the value calculated from Hall data.

A number of factors point toward the possibility of Stoner enhanced paramagnetism as the source of the discrepancy between the calculated Pauli susceptibility and the experimentally determined offset. Firstly, more than half of the component elements of the CrMnFeCoNi alloy are known to be ferromagnetic, and the work of Schneeweiss *et al.*²⁶ on this compound identify the 43 K transition as ferromagnetic, though this claim is disputed by Kamarád *et al.*²⁷. These factors suggest a proximity to magnetic order. Computational results also show a discrepancy in the spin up and spin down DOS, which indicates a spontaneous splitting of energy states. Alongside a molecular field of sufficient strength, this splitting will result in a Stoner enhancement⁷⁰.

D. Stoner Enhancement of Pauli Paramagnetism

The static component of the susceptibility is given by

$$\chi_{\text{static}} = \frac{\chi_P}{1 - Z}, \quad (12)$$

in which Z is the Stoner enhancement parameter, a value between zero and one^{70,71}. Assuming that χ_0 from the modified Curie-Weiss fit is an accurate measure of the static component of the susceptibility, the Pauli paramagnetism can be used to calculate Z . The χ_P obtained from Hall data gives a value of $Z = 0.96$. Calculating the Pauli susceptibility from the computational DOS using Eq. 11 produces a Stoner enhancement of $Z = 0.92$. Alternatively, Z can be calculated using γ , the linear component of the specific heat using Eq. 7, in combination with

$$\chi_P = \mu_0 \mu_B^2 g(E_F) \quad ^{70}, \quad (13)$$

TABLE IV: Comparison of experimentally determined Stoner enhancement parameters for multiple compounds. The Stoner parameter calculated from Eq. 9 remains at approximately 0.96 regardless of whether the core diamagnetic correction is applied.

Material	Z	Ref.
CrMnFeCoNi, Eq. 9	0.96	This work
CrMnFeCoNi, Eq. 11	0.92	This work
CrMnFeCoNi, Eq. 14	0.97	This work
Pd	0.82	⁷²⁻⁷⁵
TiBe ₂	0.91	⁷⁶
HfZn ₂	0.79	⁷⁷
YFe ₂ Zn ₂₀	0.94	⁷¹
YCo ₂ Zn ₂₀	0.50	⁷¹
WB ₄	0.93	⁷⁵

to obtain an equation for the Stoner enhancement parameter Z as a function of γ , *i.e.*

$$Z = 1 - \frac{3\mu_B^2}{\pi^2 k_B^2} \frac{\gamma}{\chi_{\text{static}}} \quad ^{71}. \quad (14)$$

Using the value of γ obtained from specific heat measurements, this expression gives a value of $Z = 0.97$. These Stoner enhancement parameters are listed alongside those of other known compounds listed in Table IV. Additionally, Leong *et al.*²³ report theoretical values for effective Stoner enhancement parameters for a number of CoCrFeNi-based high entropy alloys, all of which were found to be either ferromagnetic or close to ferromagnetic ordering.

One may observe a similarity between Eq. 14 and the Wilson ratio

$$R_W = \frac{4\pi^2 k_B^2}{3\mu_0 (g_e \mu_B)^2} \frac{\chi_0}{\gamma}, \quad (15)$$

which provides information on the electron-electron correlations in the compound, where a free electron gas has a Wilson ratio of 1 while a higher ratio indicates stronger interactions^{78,79}. The experimental results reported here give a Wilson ratio of 2.6 for the Cantor alloy anneal A sample. While this R_W is higher than the R_W of 1.2 to 2.2 observed in the strongly correlated electron compound Sr₂RuO₄, much higher Wilson ratios have been recorded⁸⁰. For example, Balents⁸¹ calculates a value of R_W as high as 230 in FeSc₂S₄ based on previously published data^{82,83}, perhaps due to competition between spin-orbit coupling and magnetic exchange, and proximity of a quantum critical point^{81,84}. Similarly, Julian *et al.*⁸⁰ calculate a Wilson ratio of approximately 40 for the nearly ferromagnetic compound Ni₃Ga, also using published data⁸⁵⁻⁸⁷.

E. Magnetic State According to the Stoner Criterion

The Stoner model of itinerant magnetism states the ferromagnetic phase should be favored if the Stoner cri-

terion, $g_0(E_F) \cdot I \geq 1$, is satisfied, where $g_0(E_F)$ is the DOS per atom at the Fermi level in the non-magnetic case (*i.e.*, from a non-spin-polarized calculation). The Stoner exchange parameter I describes the splitting between the spin-up and spin-down states in the magnetic phase. In ferromagnetic materials, the wavefunctions of the magnetic and non-magnetic state are identical, however, in the magnetic state the eigenvalues ϵ are shifted by a constant amount $\mp \frac{1}{2}IM$, where M is the magnetization^{70,88}. Thus the eigenvalues of the up and down spin states can be written as

$$\epsilon_{kv}^{\uparrow} = \epsilon_{kv}^0 - \frac{1}{2}IM, \quad (16)$$

$$\epsilon_{kv}^{\downarrow} = \epsilon_{kv}^0 + \frac{1}{2}IM, \quad (17)$$

where k and v denote the wavevectors and band indices. By subtracting Eq. 17 from Eq. 16, one finds $\Delta = (\epsilon_{kv}^{\downarrow} - \epsilon_{kv}^{\uparrow}) = IM$, which can be estimated according to the splitting of the spin up and down DOS of the magnetic system, measured in eV. Although several methods exist for determining the shift between spin-states, there is no exact or designated method, so any Stoner parameter obtained via the DOS should be considered only an approximation. In this work, the overall splitting was measured according to the average shifts in the approximate peak locations within the d -band DOS, yielding $\Delta \approx 0.233$ eV. Combined with a net magnetization of $0.294 \mu_B$, this Δ value provides a Stoner exchange parameter $I = 0.793$. To complete the Stoner criterion, the Fermi level occupation of the alloy in a non-magnetic state is needed. To obtain this value, an additional DFT simulation was performed for the equiatomic alloy in which spin-polarization effects were excluded, yielding a $g_0(E_F) = 1.663$ states/(eV · atom) for the non-magnetic alloy. Evaluation of the Stoner criterion then yields $g_0(E_F) \cdot I = 1.318$, suggesting that a weakly ferromagnetic phase should be preferred in this system.

F. Magnetic Order

The “step” in the susceptibility data visible around 43 K is roughly $1 \times 10^{-5} \mu_B \text{ atom}^{-1}$ at 0.1 kOe and 1 kOe. This transition is notable in its small size, even relative to transitions in “small-moment” ferromagnets^{89–91}. A similar transition was observed in the compound $\text{Fe}_{40}\text{Mn}_{40}\text{Co}_{10}\text{Cr}_{10}$ by Egilmez and Abuzaid⁶⁰, who identified it as ferrimagnetic and suggested that its small size was due to strong antiferromagnetic coupling between atoms.

Insight about the complex and diverse nature of the local magnetic environments is provided by DFT simulations, performed both in this work and in earlier investigations by others studying very similar alloys^{92,93}. Specifically, a sense of the variations of local magnetism

can be garnered from Fig. 12, where the local atomic magnetic moments, m , of each atom in our DFT models are plotted against the average local magnetic moment of their first nearest neighbor shells, \overline{m}_{NN} . The atoms are grouped according to species type, giving a picture of the type of coupling (*i.e.*, ferro- or antiferromagnetic) each species prefers to form with its local environment. The total magnetic moment, $p_{\text{eff}}^{\text{DFT}}$, from all four simulations, taken as the average moment of all local atomic moments was found to be $0.294 \mu_B$, which is much lower than the average magnitude (*i.e.*, disregarding spin direction) of the local moments found to be $1.103 \mu_B$. This finding indicates an uneven level of ferro- and anti-ferromagnetic couplings within the alloy, thereby providing a basis for overall (macroscopic) ferrimagnetic-like ordering.

Examining the couplings exhibited by each species in Fig. 12, one can see that the elements on the left side (*i.e.*, Cr and Mn) of the periodic table d -block tend to anti-ferromagnetically align with their local nearest neighbor shell. In other words, if the spins of an atom’s closest neighbor atoms align on average in one direction, the Cr and Mn atom spins are likely to be found aligned in the opposite direction. Conversely, Co and Ni, residing on the right side of the d -block, are more likely to align their spins ferromagnetically, or in the same direction, as the spins of their neighbors. Fe, which sits at the center of the d -block, shows neither ferro- nor anti-ferromagnetic tendencies, instead mostly aligning heavily in the spin-up direction regardless of the spins of its neighbors. It may be that the non-coupled Fe atoms are what ultimately drive the tilt in spin balance towards one direction, away from an overall anti-ferromagnetic order and into the ferrimagnetic regime.

Experimentally, the Stoner enhancement and the small magnetic moment suggest that the equiatomic Cantor alloy may be a weak itinerant ferromagnet^{94–97}. Furthermore, the magnetic component of entropy shown in the inset of Fig. 10 is approximately $0.13 R \ln 2$ at 43 K, which is an outcome reminiscent of the magnetic entropies of well-known itinerant ferromagnets ZrZn_2 and Sc_3In ($0.02 R \ln 2$ and $0.005 R \ln 2$, respectively^{98–100}). This small entropy points toward the involvement of a relatively small number of spins indicative of itinerant magnetism. Taken together with evidence of antiferromagnetic coupling from DFT calculations and modified Curie-Weiss fitting to experimental data, these pieces of evidence suggest that the equiatomic Cantor alloy is an itinerant ferrimagnet below 43 K.

V. CONCLUSION

By combining a suite of experimental techniques with numerical simulations, this work extends our understanding of the magnetic properties of the equiatomic Cantor alloy CrMnFeCoNi . Both experimental and DFT results suggest the presence of weak ferrimagnetism below about 43 K, while μSR measurements indicate a spin-glass-like

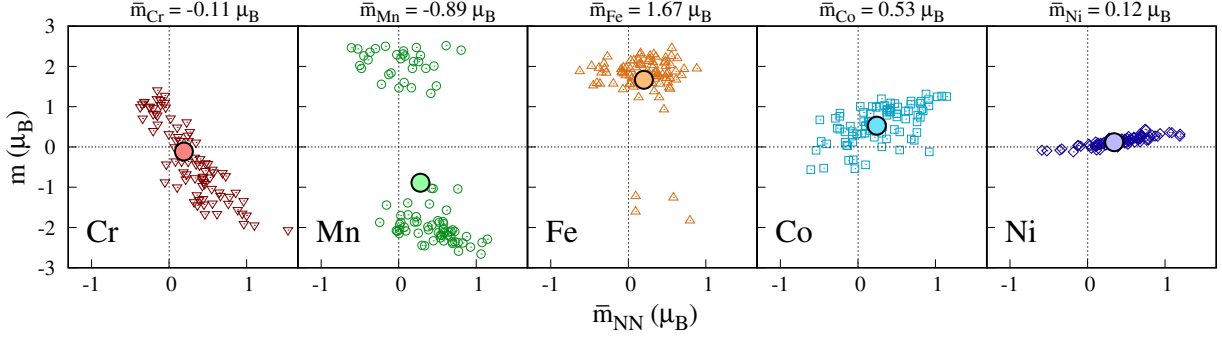


FIG. 12: The local magnetic moment of each atom is plotted against the average magnetic moment of its first nearest neighbor shell. The Y-axis depicts the local magnetic moment of each atom (*i.e.*, its spin alignment in the alloy), taken from each DFT simulation. The X-axis shows the average spin alignment of all first nearest neighbor atoms surrounding each atom. Taken together, these show how each atom type prefers to magnetically align with its environment. In the case of ferromagnetic coupling, the atom's spin aligns with its neighbors spins (*i.e.*, Co and Ni). In antiferromagnetic coupling, the atom's spin aligns in the opposite direction of its neighbor's spins (*i.e.*, Cr and Mn). The large black-outlined circle symbols designate the effective "center of mass" or average of all points for a species. The Y-value of the circle represents the average overall moment of each species type. The X-value of this circle, which is approximately the same for all species, effectively represents the overall magnetic moment of the alloy.

transition near 85 K. In addition, a large offset in the magnetic susceptibility reveals strong Stoner enhancement of the paramagnetism. Taken with the enhancement of the effective mass and the relatively large Wilson ratio, these results reveal the presence of significant electron-electron interactions within the material.

The transitions observed at 43 K and 85 K are highly sensitive to cold-working and heat treatment. Although high-temperature anneals reduce the effects of cold-working, even six-day anneals do not completely restore the sample's original magnetic properties. Despite this sensitivity, measurements on known precipitates demonstrate that these transitions are intrinsic to the compound.

This work emphasizes the need for subsequent investigations along multiple avenues. Most immediately, future work might extend Hall experiments to lower temperatures and higher fields and examine specific heat under applied magnetic field. Studies could also be undertaken to investigate the magnetic effects resulting from varying the composition of the Cantor alloy with the goal of controllably tuning the magnetic properties. Lastly, the evidence presented in this work suggests that the distinctive processing dependence of the alloy is not due to the effects of known precipitates. Lattice strain is a possible explanation, but a high-temperature anneal would be expected to eliminate strain effects. That annealing does not restore the original state of the alloy suggests the presence of a mechanism that will require further research to elucidate.

VI. ACKNOWLEDGMENTS

Synthesis and characterization facilities at the University of Florida were developed under support from NSF-

CAREER 1453752 (J.J.H.). J.J.H. benefited from enlightening conversations with D.L. Maslov. B.A.F. and E.Z. acknowledge support from the College of Physical and Mathematical Sciences at Brigham Young University and also thank the scientific staff at the Centre for Molecular and Materials Science at TRIUMF for support during the muon spin relaxation experiment. A portion of this work was performed at the National High Magnetic Field Laboratory, which is supported by the National Science Foundation Cooperative Agreement No. DMR-1644779 and the State of Florida. The authors acknowledge the staff of the Nano Research Facility at University of Florida for their assistance and guidance in acquiring SEM and XRD data.

The computational work was performed, in part, at the Center for Integrated Nanotechnologies, an Office of Science User Facility operated for the U.S. Department of Energy. Sandia National Laboratories is a multi-mission laboratory managed and operated by National Technology & Engineering Solutions of Sandia, LLC, a wholly owned subsidiary of Honeywell International Inc., for the U.S. Department of Energy's National Nuclear Security Administration under contract DE-NA0003525. This paper describes objective technical results and analysis. Any subjective views or opinions that might be expressed in the paper do not necessarily represent the views of the U.S. Department of Energy or the United States Government.

- ¹ B. Cantor, K. B. Kim, and P. J. Warren, Novel multicomponent amorphous alloys, in *Metastable, Mechanically Alloyed and Nanocrystalline Materials* (Materials Science Forum, Vol. 386 (Trans Tech Publications Ltd, 2002) pp. 27–32.
- ² J.-W. Yeh, S.-K. Chen, S.-J. Lin, J.-Y. Gan, T.-S. Chin, T.-T. Shun, C.-H. Tsau, and S.-Y. Chang, Nanostructured high-entropy alloys with multiple principal elements: Novel alloy design concepts and outcomes, *Advanced Engineering Materials* **6**, 299 (2004).
- ³ G. S. Firstov, T. A. Kosorukova, Y. N. Koval, and V. V. Odnosum, High Entropy Shape Memory Alloys, *Materials Today: Proceedings International Conference on Materials Science and Engineering* **160**, 1499 (2015).
- ⁴ C.-H. Chen and Y.-J. Chen, Shape memory characteristics of (TiZrHf)₅₀Ni₂₅Co₁₀Cu₁₅ high entropy shape memory alloy, *Scripta Materialia* **162**, 185 (2019).
- ⁵ K. Motla, Arushi, P. K. Meena, and R. P. Singh, Boron based new high entropy alloy superconductor Mo_{0.11}W_{0.11}V_{0.11}Re_{0.34}B_{0.33}, *arXiv:2201.03300 [cond-mat]* (2022), arXiv: 2201.03300.
- ⁶ Y. Zhang, T. Zuo, Y. Cheng, and P. K. Liaw, High-entropy alloys with high saturation magnetization, electrical resistivity and malleability, *Scientific Reports* **3**, 1455 (2013).
- ⁷ T. Zuo, M. C. Gao, L. Ouyang, X. Yang, Y. Cheng, R. Feng, S. Chen, P. K. Liaw, J. A. Hawk, and Y. Zhang, Tailoring magnetic behavior of CoFeMnNi_x (X = Al, Cr, Ga, and Sn) high entropy alloys by metal doping, *Acta Materialia* **130**, 10 (2017).
- ⁸ B. Cantor, I. T. H. Chang, P. Knight, and A. J. B. Vincent, Microstructural development in equiatomic multicomponent alloys, *Materials Science and Engineering: A* **375–377**, 213 (2004).
- ⁹ F. Otto, A. Dlouhý, C. Somsen, H. Bei, G. Eggeler, and E. P. George, The influences of temperature and microstructure on the tensile properties of a CoCrFeMnNi high-entropy alloy, *Acta Materialia* **61**, 5743 (2013).
- ¹⁰ M. Laurent-Brocq, A. Akhatova, L. Perrière, S. Chebini, X. Sauvage, E. Leroy, and Y. Champion, Insights into the phase diagram of the CrMnFeCoNi high entropy alloy, *Acta Materialia* **88**, 355 (2015).
- ¹¹ M. J. Jang, S. Praveen, H. J. Sung, J. W. Bae, J. Moon, and H. S. Kim, High-temperature tensile deformation behavior of hot rolled CrMnFeCoNi high-entropy alloy, *Journal of Alloys and Compounds* **730**, 242 (2018).
- ¹² J. H. Kim, K. R. Lim, J. W. Won, Y. S. Na, and H.-S. Kim, Mechanical properties and deformation twinning behavior of as-cast CoCrFeMnNi high-entropy alloy at low and high temperatures, *Materials Science and Engineering: A* **712**, 108 (2018).
- ¹³ S.-W. Kim and J. H. Kim, In-situ observations of deformation twins and crack propagation in a CoCrFeNiMn high-entropy alloy, *Materials Science and Engineering: A* **718**, 321 (2018).
- ¹⁴ X. F. Wang, Y. Zhang, F. Qiao, and G. L. Chen, Novel microstructure and properties of multicomponent CoCrCuFeNiTi_x alloys, *Intermetallics* **15**, 357 (2007).
- ¹⁵ K. B. Zhang, Z. Y. Fu, J. Y. Zhang, J. Shi, W. M. Wang, H. Wang, Y. C. Wang, and Q. J. Zhang, Annealing on the structure and properties evolution of the CoCrFeNiCuAl high-entropy alloy, *Journal of Alloys and Compounds* **502**, 295 (2010).
- ¹⁶ Y.-F. Kao, S.-K. Chen, T.-J. Chen, P.-C. Chu, J.-W. Yeh, and S.-J. Lin, Electrical, magnetic, and Hall properties of Al_xCoCrFeNi high-entropy alloys, *Journal of Alloys and Compounds* **509**, 1607 (2011).
- ¹⁷ M. S. Lucas, L. Mauger, J. A. Muñoz, Y. Xiao, A. O. Sheets, S. L. Semiatin, J. Horwath, and Z. Turgut, Magnetic and vibrational properties of high-entropy alloys, *Journal of Applied Physics* **109**, 07E307 (2011).
- ¹⁸ S. Singh, N. Wanderka, K. Kiefer, S. Siemensmeyer, and J. Banhart, Effect of decomposition of the Cr–Fe–Co rich phase of AlCoCrCuFeNi high entropy alloy on magnetic properties, *Intermetallics* **60**, 1499 (2015).
- ¹⁹ L. Liu, J. B. Zhu, J. C. Li, and Q. Jiang, Microstructure and magnetic properties of FeNiCuTi_x high entropy alloys, *Advanced Engineering Materials* **14**, 919 (2012).
- ²⁰ S. G. Ma and Y. Zhang, Effect of Nb addition on the microstructure and properties of AlCoCrFeNi high-entropy alloy, *Materials Science and Engineering: A* **532**, 480 (2012).
- ²¹ K. Zhang and Z. Fu, Effects of annealing treatment on properties of CoCrFeNiTiAl_x multi-component alloys, *Intermetallics* **28**, 34 (2012).
- ²² M.-H. Tsai, Physical properties of high entropy alloys, *Entropy* **15**, 5338 (2013).
- ²³ Z. Leong, J. S. Wróbel, S. L. Dudarev, R. Goodall, I. Todd, and D. Nguyen-Manh, The effect of electronic structure on the phases present in high entropy alloys, *Scientific Reports* **7**, 39803 (2017).
- ²⁴ K. Jin, B. C. Sales, G. M. Stocks, G. D. Samolyuk, M. Daene, W. J. Weber, Y. Zhang, and H. Bei, Tailoring the physical properties of Ni-based single-phase equiatomic alloys by modifying the chemical complexity, *Scientific Reports* **6**, 20159 (2016).
- ²⁵ P. F. Yu, L. J. Zhang, H. Cheng, H. Zhang, M. Z. Ma, Y. C. Li, G. Li, P. K. Liaw, and R. P. Liu, The high-entropy alloys with high hardness and soft magnetic property prepared by mechanical alloying and high-pressure sintering, *Intermetallics* **70**, 82 (2016).
- ²⁶ O. Schneeweiss, M. Friák, M. Dudová, D. Holec, M. Šob, D. Kriegner, V. Holý, P. Beran, E. P. George, J. Neugebauer, and A. Dlouhý, Magnetic properties of the CrMnFeCoNi high-entropy alloy, *Physical Review B* **96**, 014437 (2017).
- ²⁷ J. Kamarád, M. Friák, J. Kaštil, O. Schneeweiss, M. Šob, and A. Dlouhý, Effect of high pressure on magnetic properties of CrMnFeCoNi high entropy alloy, *Journal of Magnetism and Magnetic Materials* **487**, 165333 (2019).
- ²⁸ D. Billington, A. D. N. James, E. I. Harris-Lee, D. A. Lagos, D. O'Neill, N. Tsuda, K. Toyoki, Y. Kotani, T. Nakamura, H. Bei, S. Mu, G. D. Samolyuk, G. M. Stocks, J. A. Duffy, J. W. Taylor, S. R. Giblin, and S. B. Dugdale, Bulk and element-specific magnetism of medium-entropy and high-entropy Cantor-Wu alloys, *Physical Review B* **102**, 174405 (2020).
- ²⁹ G. E. Bacon and N. Cowlam, Magnetic studies of annealed and alloyed chromium by neutron diffraction, *Journal of Physics C: Solid State Physics* **2**, 238 (1969).
- ³⁰ L. Patrick, Antiferromagnetism of manganese, *Physical Review* **93**, 370 (1954).
- ³¹ J. R. Rumble, ed., *CRC Handbook of Chemistry and*

- Physics*, 102nd ed. (CRC Press, Boca Raton London New York, 2021).
- ³² S. J. Blundell, Spin-polarized muons in condensed matter physics, *Contemporary Physics* **40**, 175 (2010).
 - ³³ A. Suter and B. Wojek, Musrfit: A free platform-independent framework for musr data analysis, *Physics Procedia* **30**, 69 (2012), 12th International Conference on Muon Spin Rotation, Relaxation and Resonance (μ SR2011).
 - ³⁴ K. A. Petersen, J. Black, and B. A. Frandsen, Beams: Basic and effective analysis for muon spin spectroscopy (2021).
 - ³⁵ A. Yaouanc and P. D. de Réotier, *Muon Spin Rotation, Relaxation, and Resonance: Applications to Condensed Matter*, 1st ed. (Oxford University Press, Oxford, 2011).
 - ³⁶ G. Kresse and J. Hafner, Ab initio molecular dynamics for liquid metals, *Phys. Rev. B* **47**, 558 (1993).
 - ³⁷ G. Kresse and J. Hafner, Ab initio molecular-dynamics simulation of the liquid-metalamorphous- semiconductor transition in germanium, *Phys. Rev. B* **49**, 14251 (1994).
 - ³⁸ G. Kresse, Ab initio molecular dynamics for liquid metals, *J. Non-Cryst. Solids* **192-193**, 222 (1995).
 - ³⁹ P. E. Blochl, Projector augmented-wave method, *Phys. Rev. B* **50**, 17979 (1994).
 - ⁴⁰ G. Kresse and D. Joubert, From ultrasoft pseudopotentials to the projector augmented-wave method, *Phys. Rev. B* **59**, 1758 (1999).
 - ⁴¹ J. P. Perdew, K. Burke, and M. Ernzerhof, Generalized gradient approximation made simple, *Phys. Rev. Lett.* **77**, 3865 (1996).
 - ⁴² S. H. Wei, L. G. Ferreira, J. E. Bernard, and A. Zunger, Electronic properties of random alloys: special quasirandom structures, *Phys. Rev. B* **42**, 9622 (1990).
 - ⁴³ A. Zunger, S. H. Wei, L. G. Ferreira, and J. E. Bernard, Special quasirandom structures, *Phys. Rev. Lett.* **65**, 353 (1990).
 - ⁴⁴ A. van de Walle, P. Tiwary, M. M. de Jong, D. L. Olmsted, M. D. Asta, A. Dick, D. Shin, Y. Wang, L. Q. Chen, and Z. K. Liu, Efficient stochastic generation of special quasirandom structures, *Calphad* **42**, 13 (2013).
 - ⁴⁵ E. J. Pickering, R. Muñoz-Moreno, H. J. Stone, and N. G. Jones, Precipitation in the equiatomic high-entropy alloy CrMnFeCoNi, *Scripta Materialia* **113**, 106 (2016).
 - ⁴⁶ F. Otto, A. Dlouhý, K. G. Pradeep, M. Kuběnová, D. Raabe, G. Eggeler, and E. P. George, Decomposition of the single-phase high-entropy alloy CrMnFeCoNi after prolonged anneals at intermediate temperatures, *Acta Materialia* **112**, 40 (2016).
 - ⁴⁷ F. Otto, N. L. Hanold, and E. P. George, Microstructural evolution after thermomechanical processing in an equiatomic, single-phase CoCrFeMnNi high-entropy alloy with special focus on twin boundaries, *Intermetallics* **54**, 39 (2014).
 - ⁴⁸ A. Gali and E. P. George, Tensile properties of high- and medium-entropy alloys, *Intermetallics* **39**, 74 (2013).
 - ⁴⁹ M. McElfresh, *Fundamentals of Magnetism and Magnetic Measurements* (Quantum Design, 1994).
 - ⁵⁰ B. Schuh, F. Mendez-Martin, B. Völker, E. P. George, H. Clemens, R. Pippan, and A. Hohenwarter, Mechanical properties, microstructure and thermal stability of a nanocrystalline CoCrFeMnNi high-entropy alloy after severe plastic deformation, *Acta Materialia* **96**, 258 (2015).
 - ⁵¹ Y. J. Li, A. Savan, A. Kostka, H. S. Stein, and A. Ludwig, Accelerated atomic-scale exploration of phase evolution in compositionally complex materials, *Materials Horizons* **5**, 86 (2018).
 - ⁵² Y. Uemura, μ sr relaxation functions in magnetic materials, in *Muon Science: Muons in Physics, Chemistry and Materials*, edited by S. Lee, R. Cywinski, and S. Kilcoyne (Taylor & Francis, New York, 1999).
 - ⁵³ R. Crook, M. R. Cywinski, Voigtian kubo - toyabe muon spin relaxation, *J. Phys.: Condens. Matter* **9**, 1149 (1997).
 - ⁵⁴ Y. J. Uemura, T. Yamazaki, D. R. Harshman, M. Senba, and E. J. Ansaldo, Muon-spin relaxation in aFe and CuNi spin glasses, *Phys. Rev. B* **31**, 546 (1985).
 - ⁵⁵ S. R. Dunsiger, R. F. Kiefl, K. H. Chow, B. D. Gaulin, M. J. P. Gingras, J. E. Greedan, A. Keren, K. Kojima, G. M. Luke, W. A. MacFarlane, N. P. Raju, J. E. Sonier, Y. J. Uemura, and W. D. Wu, Muon spin relaxation investigation of the spin dynamics of geometrically frustrated antiferromagnets Y₂Mo₂O₇ and Tb₂Mo₂O₇, *Phys. Rev. B* **54**, 9019 (1996).
 - ⁵⁶ B. A. Frandsen, K. A. Petersen, N. A. Ducharme, A. G. Shaw, E. J. Gibson, B. Winn, J. Yan, J. Zhang, M. E. Manley, and R. P. Hermann, Spin dynamics and a nearly continuous magnetic phase transition in an entropy-stabilized oxide antiferromagnet, *Phys. Rev. Materials* **4**, 074405 (2020).
 - ⁵⁷ A. Tari, *The Specific Heat of Matter at Low Temperatures* (Imperial College Press; Distributed by World Scientific Pub. Co, London: River Edge, NJ, 2003).
 - ⁵⁸ N. W. Ashcroft and N. D. Mermin, *Solid state physics* (Holt, Rinehart and Winston, New York, 1976).
 - ⁵⁹ J. Singleton, *Band theory and electronic properties of solids*, Oxford master series in condensed matter physics (Oxford University Press, Oxford ; New York, 2001).
 - ⁶⁰ M. Egilmez and W. Abuzaid, Magnetic, electrical and mechanical properties of Fe₄₀Mn₄₀Co₁₀Cr₁₀ high entropy alloy, *Scientific Reports* **11**, 8048 (2021).
 - ⁶¹ D. V. Schroeder, *An Introduction to Thermal Physics*, internat. ed. (Addison Wesley, San Francisco, Calif., 2000).
 - ⁶² C. Kittel, *Introduction to Solid State Physics*, 8th ed. (J. Wiley & sons, New York, 2005).
 - ⁶³ J. B. Austin, Heat capacity of iron - a review, *Industrial & Engineering Chemistry* **24**, 1225 (1932).
 - ⁶⁴ W. H. Keesom and B. Kurelmeyer, The atomic heat of iron from 1.1 to 20.4 °K, *Physica* **6**, 633 (1939).
 - ⁶⁵ K. K. Kelley, The specific heat of pure iron at low temperatures, *The Journal of Chemical Physics* **11**, 16 (1943).
 - ⁶⁶ J. M. Ziman, *Principles of the Theory of Solids*, 2nd ed. (University Press, Cambridge [Eng.], 1972).
 - ⁶⁷ B. Hammer and J. K. Nørskov, Why gold is the noblest of all the metals, *Nature* **376**, 238 (1995).
 - ⁶⁸ L. N. Mulay, E. A. Boudreaux, et al., *Theory and applications of molecular diamagnetism* (Wiley, 1976).
 - ⁶⁹ G. A. Bain and J. F. Berry, Diamagnetic corrections and pascal's constants, *Journal of Chemical Education* **85**, 532 (2008).
 - ⁷⁰ S. J. Blundell, *Magnetism in Condensed Matter* (Oxford University Press, Oxford, New York, 2001).
 - ⁷¹ S. Jia, S. L. Bud'ko, G. D. Samolyuk, and P. C. Canfield, Nearly ferromagnetic Fermi-liquid behaviour in YFe₂Zn₂₀ and high-temperature ferromagnetism of GdFe₂Zn₂₀, *Nature Physics* **3**, 334 (2007).
 - ⁷² F. E. Hoare, J. C. Matthews, J. C. Walling, and E. C. Stoner, The thermal and magnetic properties of palladium-silver alloys,

- Proceedings of the Royal Society of London. Series A. Mathematical and Physical Sciences **216**, 1021 (1953).
- ⁷³ G. Chouteau, R. Fourneaux, K. Gobrecht, and R. Tournier, Specific heat and susceptibility enhancement in dilute Pd: Ni alloys, *Physical Review Letters* **20**, 193 (1968).
 - ⁷⁴ S. C. Hong, T. H. Rho, and J. Il Lee, Enhancement of magnetic moment by interface effect: Co/Pd(111), *Journal of Magnetism and Magnetic Materials International Conference* **140**, 144 (1995).
 - ⁷⁵ J. Shen, J. Zhou, M. Zhao, G. Liu, J. Gao, and J. Yao, Stoner-enhanced paramagnetism in tungsten tetraboride, *Journal of Physics: Condensed Matter* **28**, 026005 (2016).
 - ⁷⁶ G. R. Stewart, J. L. Smith, A. L. Giorgi, and Z. Fisk, Specific heat of well-characterized TiBe₂ at 0 and 7 T, *Physical Review B* **25**, 5907 (1982).
 - ⁷⁷ H. B. Radousky, G. S. Knapp, J. W. Downey, A. T. Aldred, and A. J. Freeman, Magnetic properties of HfZn₂, *Journal of Magnetism and Magnetic Materials* **40**, 117 (1983).
 - ⁷⁸ J. Sólyom, *Fundamentals of the Physics of Solids* (Springer, Berlin, 2009).
 - ⁷⁹ U. B. Paramanik, Anupam, U. Burkhardt, R. Prasad, C. Geibel, and Z. Hos-sain, Valence fluctuation in CeMo₂Si₂C, *Journal of Alloys and Compounds* **580**, 435 (2013).
 - ⁸⁰ S. R. Julian, A. P. Mackenzie, G. G. Lonzarich, C. Bergemann, R. K. W. Haselwimmer, Y. Maeno, S. NishiZaki, A. W. Tyler, S. Ikeda, and T. Fujita, Normal state, superconductivity and quasiparticle Fermi surface of the strongly correlated oxide Sr₂RuO₄, *Physica B: Condensed Matter* **259-261**, 928 (1999).
 - ⁸¹ L. Balents, Spin liquids in frustrated magnets, *Nature* **464**, 199 (2010).
 - ⁸² N. Büttgen, A. Zymara, C. Kegler, V. Tsurkan, and A. Loidl, Spin and orbital frustration in FeSc₂S₄ probed by ⁴⁵Sc NMR, *Physical Review B* **73**, 132409 (2006).
 - ⁸³ V. Fritsch, J. Hemberger, N. Büttgen, E.-W. Scheidt, H.-A. Krug von Nidda, A. Loidl, and V. Tsurkan, Spin and orbital frustration in MnSc₂S₄ and FeSc₂S₄, *Physical Review Letters* **92**, 116401 (2004).
 - ⁸⁴ G. Chen, L. Balents, and A. P. Schnyder, Spin-orbital singlet and quantum critical point on the diamond lattice: FeSc₂S₄, *Physical Review Letters* **102**, 096406 (2009).
 - ⁸⁵ W. d. Dood and P. F. d. Chatel, Low temperature specific heat of Ni₃Al and Ni₃Ga, *Journal of Physics F: Metal Physics* **3**, 1039 (1973).
 - ⁸⁶ C. J. Schinkel, F. R. d. Boer, and B. d. Hon, The applicability of the Stoner-Edwards-Wohlfarth model to Ni₃ Ga, *Journal of Physics F: Metal Physics* **3**, 1463 (1973).
 - ⁸⁷ S. M. Hayden, G. G. Lonzarich, and H. L. Skriver, Electronic structure of the strongly-exchange-enhanced paramagnet Ni₃Ga, *Physical Review B* **33**, 4977 (1986).
 - ⁸⁸ R. Zeller, Spin-polarized dft calculations and magnetism, John von Neumann Institute for Computing (John von Neumann Institute for Computing, 2006) pp. 419–445.
 - ⁸⁹ A. P. Murani, A. Tari, and B. R. Coles, Critical concentration for the onset of ferromagnetism in Pd-Ni alloys, *Journal of Physics F: Metal Physics* **4**, 1769 (1974).
 - ⁹⁰ E. A. Yelland, S. J. C. Yates, O. Taylor, A. Griffiths, S. M. Hayden, and A. Carrington, Ferromagnetic properties of ZrZn₂, *Physical Review B* **72**, 184436 (2005).
 - ⁹¹ S. M. Saunders, L. Xiang, R. Khasanov, T. Kong, Q. Lin, S. L. Bud'ko, and P. C. Canfield, Exceedingly small moment itinerant ferromagnetism of single crystalline La₅Co₂Ge₃, *Physical Review B* **101**, 214405 (2020).
 - ⁹² C. Niu, A. J. Zaddach, A. A. Oni, X. Sang, J. W. Hurt, and M. H. Physica Scripta **2021**, 021103 (2021).
 - ⁹³ C. Niu, C. R. LaRosa, J. Miao, M. J. Mills, and M. Ghazisaeidi, Magnetically-driven phase transformation strengthening in high entropy alloys, *Nature Communications* **9**, 1363 (2018).
 - ⁹⁴ S. Ogawa and N. Sakamoto, Magnetic properties of ZrZn₂-itinerant electron ferromagnet, *Journal of the Physical Society of Japan* **22**, 1214 (1967).
 - ⁹⁵ G. S. Knapp, F. Y. Fradin, and H. V. Culbert, Ferromagnetism of ZrZn₂, *Journal of Applied Physics* **42**, 1341 (1971).
 - ⁹⁶ P. G. Mattocks and D. Melville, The magnetic properties of high-purity ZrZn₂ in pulsed fields of up to 17 T, *Journal of Physics F: Metal Physics* **8**, 1291 (1978).
 - ⁹⁷ M. D. Vannette and R. Prozorov, Field-dependent AC susceptibility of itinerant ferromagnets, *Journal of Physics: Condensed Matter* **20**, 475208 (2008).
 - ⁹⁸ R. Viswanathan, Magnetic entropy of ZrZn₂, *Journal of Physics F: Metal Physics* **4**, L57 (1974).
 - ⁹⁹ J. R. Clinton and R. Viswanathan, Magnetization and magnetic entropy of ZrZn₂, *Journal of Magnetism and Magnetic Materials* **1**, 73 (1975).
 - ¹⁰⁰ G. S. Knapp, L. L. Isaacs, H. V. Culbert, and R. A. Conner, The resistivity and specific heat of ferromagnetic Sc₃In, *AIP Conference Proceedings* **5**, 467 (1972).